Correspondence to:
Ø. Breivik,
oyvind.breivik@met.no

Long-Term Statistics of Observed Bubble Depth Versus Modeled Wave Dissipation

Kjersti Opstad Strand[1] , Øyvind Breivik[1,2] , Geir Pedersen[3,4] , Frode Bendiksen Vikebø[3,5], Svein Sundby[3], and Kai Håkon Christensen[1,6]

[1]Norwegian Meteorological Institute, Oslo, Norway, [2]Geophysical Institute, University of Bergen, Bergen, Norway, [3]Institute of Marine Research, Bergen, Norway, [4]NORCE Norwegian Research Centre, Bergen, Norway, [5]Bjerknes Centre of Climate Research, Bergen, Norway, [6]Department of Geosciences, University of Oslo, Oslo, Norway

Abstract Air bubble penetration depths are investigated with a bottom-mounted echosounder at a seabed observatory in northern Norway. We compare a 1-year time series of observed bubble depth against modeled and estimated turbulent kinetic energy flux from breaking waves as well as wind speed and sea state. We find that the hourly mean and maximum bubble depths are highly variable, reaching 18 and 38 m, respectively, and strongly correlated with wind and sea state. The bubble depth is shallowest during summer following the seasonal variations in wind speed and wave height. Summertime shallowing of the mixed layer depth is not limiting the penetration depth. A strong relationship between bubble depth and modeled turbulent kinetic energy flux from breaking waves is found, similar in strength to the relationship between bubble depth and wind speed. The wind sea is more strongly correlated with bubble depth than the total significant wave height, and the swell is only weakly correlated, suggesting that the wave model does a reasonable separation of swell and wind sea.

Plain Language Summary Down-mixed air bubbles measured with a bottom-based echosounder provide an opportunity to observe upper ocean processes continuously through all types of weather. Here we investigate the correlation between air bubble depth and modeled energy flux from breaking waves. We investigate 1 year of data available from an offshore location in Northern Norway. Results show that the hourly mean and maximum bubble depths are highly variable, reaching 18 and 38 m, respectively, and strongly correlated with wind and sea state. The bubble depth is shallowest during summer, following the seasonal variations in wind and wave height. We find that the bubble depth is not limited by the depth of the mixed layer. A relationship between bubble depth and energy flux is found, similar to the relationship between wind and energy flux. This is important for prediction of both dispersal of particles (such as oil spills and marine plankton) and transfer of gases from the atmosphere to the ocean.

1. Introduction

Breaking surface waves generate turbulent mixing and entrain air bubbles in the water column (Gemmrich & Farmer, 1999; Thomson et al., 2016; Thorpe, 1982). This controls the air-sea gas exchange crucial for the ventilation of the ocean and the uptake of carbon dioxide and oxygen (Rhein et al., 2013). Quantifying these fluxes is essential for modeling of the air-sea interaction and its role in coupled Earth system models (Breivik et al., 2015; Fan & Griffies, 2014). This in turn has consequences for anthropogenic emissions as these fluxes determine the properties of the ocean mixed layer and the absorption of gases (Zappa et al., 2007).

While the wind stress acting on the sea surface in the open ocean causes mixing of diffused gases by shear-driven turbulence and wave generation (and thereby also Langmuir circulation), it is only when waves break that there is direct entrainment of gas into the ocean (Bell et al., 2017; Zappa et al., 2007) in the form of bubbles. To realistically model air-sea gas exchange, numerical models must be able to represent the flux of wave-generated turbulent kinetic energy (TKE). Recent studies have parameterized wave-generated turbulence in ocean models, with the purpose of improving the representation of ocean surface temperature and the mixed-layer depth (Alari et al., 2016; Breivik et al., 2015; Burchard, 2001; Mellor & Blumberg, 2004; Staneva et al., 2017; Wu, Staneva et al. 2019; Wu, Rutgersson, et al. 2019).

Several ocean and wave model studies (Ali et al., 2019; Belcher et al., 2012; Breivik et al., 2019; Li et al., 2017) and fully coupled atmosphere-wave-ocean climate models (Breivik et al., 2015; Fan & Griffies, 2014;

Li et al., 2016) have investigated the relationship between Langmuir turbulence and upper ocean mixing and how this may change under a changing climate. It is clear that Langmuir turbulence will enhance the vertical extent of the air-sea gas exchange brought about by wave breaking and thus affect the vertical distribution of buoyant particles. It is however not clear how deep into the mixed layer buoyant particles may be brought by wave-generated and shear-generated turbulence. Knowing the vertical distribution of buoyant particles is crucial when predicting dispersal since horizontal currents vary with depth, whether the particles in question are air bubbles (Thorpe, 1992), buoyant fish eggs (Sundby, 1983), or oil droplets (Jones et al., 2016; Paris et al., 2012). The challenge in addressing these issues is often due to measurement limitations, both for observing processes and for model validation. Our aim with this paper is to exploit continuous acoustic data to investigate the relationship between turbulent mixing by breaking waves and the air bubble distribution in the upper ocean.

Down-mixed air bubbles scatter sound waves and can be observed by echo sounding instruments (Thorpe, 1982). Such instruments, initially used for mapping the ocean sea floor, detecting submarines and assisting fisheries (Sund, 1935), are now widely used in physical oceanography (Colbo et al., 2014). In the past four decades echosounders have been used to study various dynamic processes in the upper ocean (see early work by Thorpe, 1982, 1984, 1992; Vagle & Farmer, 1992 and more recent work by Trevorrow, 2003 and Wang et al., 2016). There is an ongoing debate about the turbulent dissipation near the ocean surface and whether the law-of-the-wall scaling is valid in this zone (Craig & Banner, 1994; Esters et al., 2018; Terray et al., 1996, 1997). Some of this work is based on observations of bubble clouds (Thorpe, 1992; Wang et al., 2016). It is nevertheless clear that the law-of-the-wall scaling does not hold in the breaking zone (Fisher et al., 2018; Gemmrich, 2010; Sutherland & Melville, 2015; Thomson et al., 2016; Zippel et al., 2018). Vertical size-specific bubble distributions for radii between 8 and 130 µm were measured by Vagle and Farmer (1992) using a multifrequency acoustic backscatter technique. Such detailed bubble distributions allow estimates of the total amount of air entrained by breaking waves and the associated gas transfer. Air-sea gas fluxes are usually parameterized in terms of a gas transfer velocity, which is typically taken to depend on wind speed. Efforts to link the gas transfer velocity directly to turbulence dissipation rates (Lamont & Scott, 1970; Zappa et al., 2007) are promising, but there are still uncertainties due to a lack of dissipation measurements very close to the surface (Esters et al., 2017).

Here we investigate the relation between the measured bubble penetration depth and the modeled TKE flux from breaking waves. The recent work by Callaghan et al. (2016) and Callaghan (2018) shows a new framework for bubble volume as a proxy for dissipation, connecting whitecapping and bubble penetration depth. As shown by Callaghan (2018), the missing link in defining a relationship between the energy dissipation rate associated with whitecaps is the bubble plume penetration depth. For the first time a yearlong series of bubble depths measured with an upward looking echosounder is compiled and analyzed. Following the procedure of Thorpe (1992), Trevorrow (2003), and Wang et al. (2016), we investigate how the bubble depth varies with surface wind speed and sea state (represented by significant wave height, swell, wind sea, and the amount of wave breaking). We assess the relation between observed bubble depth and the TKE flux from breaking waves from the wave model EC-WAM (ECMWF, 2019). In particular, we address the following questions: (i) how far down do air bubbles penetrate and what is the seasonal variation, (ii) how does bubble depth relate to wind and sea state, and finally (iii) how does the modeled TKE flux correlate with measured bubble depth?

This paper is organized as follows. The observatory, the echosounder instrument, other observations, and the wave model are presented in sections 2 and 3. The observed relationship between bubble depth and modeled wind and wave parameters is presented in section 4. The results are discussed, and conclusions are presented in sections 5 and 6. An assessment of the echosounder′s ability to measure significant wave height is presented in Appendix A.

2. Observations

We have compiled measurements over a 1-year period (14 November 2014 to 18 November 2015) north of the Lofoten archipelago in Northern Norway (between 67° and 68°N, centered around 14°E; see Figure 1). Observations include acoustic data from an upward looking echosounder located at the Lofoten-Vesterålen (hereafter LoVe) Ocean Observatory, meteorological observations from Andøya and Røst, and observed hydrography at Eggum.
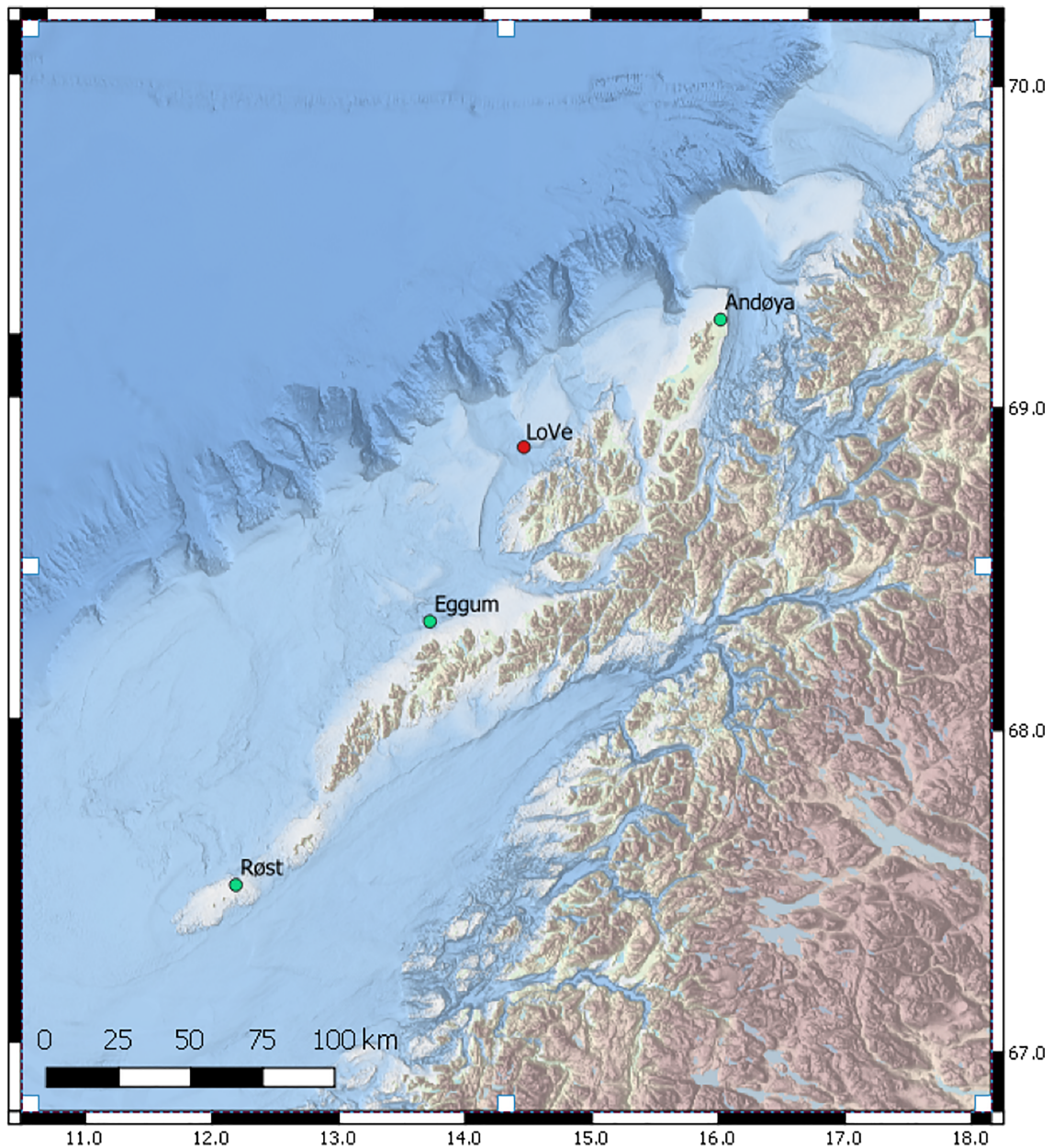
Figure 1. Location of the LoVe Ocean Observatory; the two meteorological stations, Røst and Andøya, and the hydrological station, Eggum.

Located north of the Arctic Circle, the study area undergoes a period of near complete darkness during winter and strong biological productivity during spring. The Norwegian continental shelf is at its narrowest near the LoVe site, linking the near-shore continental shelf strongly to the deep Norwegian Sea, where the most important zooplankton species in the area, *Calanus finmarchicus*, overwinter in the deep (e.g., Melle & Skjoldal, 1998; Melle et al., 2004). Periods of high biological primary and secondary production give strong backscatter throughout the water column and will be considered as a possible contaminating factor when investigating the echosounder measurements.

The site is exposed to the open ocean at a location with frequent passages of extratropical storm systems from the southwest with associated significant wave height in excess of 12 m (Aarnes et al., 2012; Breivik et al., 2013). The depth is more than 250 m, making it a deepwater site in terms of the wave dispersion relation (see Figure 1).
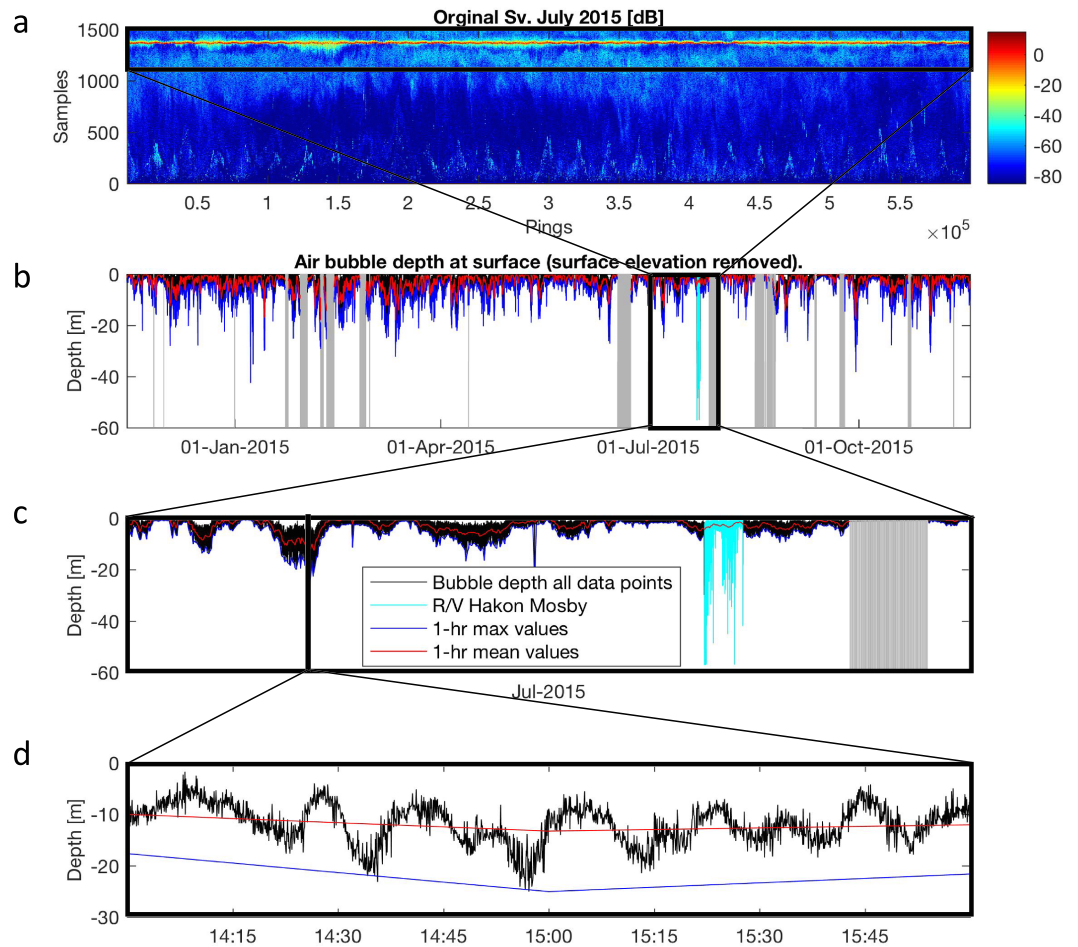
Figure 2. (a) Raw data from the upward looking echosounder (EK60). The *x* axis shows time as the number of samples during the month of July 2015. The *y* axis shows the amount of samples starting counting from the echosounder transducer to the ocean surface. The sample range is around 19 cm. (b) The filtered bubble layer depth at the LoVe ocean observatory for the whole data set 14–18 November 2015. (c) Zoom of July 2015, the same month as in panel (a). The black line is maximum air bubble depth, red is the hourly mean, while green is the hourly maximum. The cyan line shows the signal from R/V Håkon Mosby as it passed through the area (since removed from the data set). Gray shading in (a) and (b) indicates missing data. (d) A 2-hr zoom of the bubble depth during a high wind situation. There is a marked periodicity to the bubble penetration depth which is attributed to wind gustiness and the natural groupiness of waves. The red and blue lines indicate the mean and maximum bubble depth (linearly interpolated), respectively.

2.1. The EK60 Echosounder

The permanent LoVe Observatory located outside Vesterålen (Figure 1) has a 70 kHz bottom-mounted narrow band split beam (7°) echosounder (Simrad EK60). The frame is placed at 258-m depth and has a 31-m surface detection diameter. Sampling frequency is 0.25 Hz with a vertical sample resolution of 0.19 m. The echosounder was calibrated using a tungsten carbide calibration sphere (WC38.1), according to best practice for calibration of scientific echosounders, using the standard sphere method (Demer et al., 2015; Foote, 1987). A time variable gain function is applied to compensate the received echo data for the loss of acoustic energy due to geometric spread and absorption. Backscatter intensity from July 2015 is shown in Figure 2a. Air bubble backscatter depends on the product of acoustic wavenumber, a quantity proportional to the acoustic frequency, and the dimension of the scatterer (the bubble). Assuming spherical bubbles and using mass and stiffness equations (see, e.g., Clay & Medwin, 1977), the radius of resonating bubbles at 70 kHz close to the surface is estimated to be about 45 μm, increasing to 85 μm at 30-m depth. Since ours is a single-frequency instrument with a sampling frequency of 0.25 Hz, the observed signal will come from resonant bubbles of differing radii (depending on depth) that remain in the water column for more than 4 s. The echosounder is also able to measure significant wave height, as we present in Appendix A. However, its
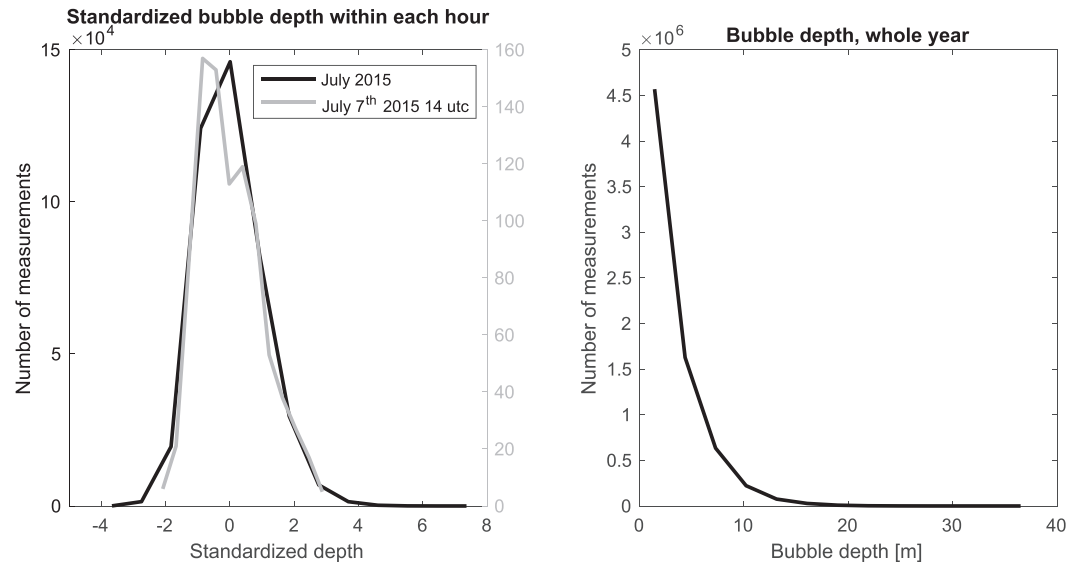
Figure 3. Left panel: The histogram of standardized depth within each hour for the data shown in Figures 2c and 2d (black curve represents the month of July),and 1 hr (gray curve represents 2015-07-07T14UTC) shown in Figure 2d). The intrahourly data follow a weak lognormal distribution slightly skewed toward higher bubble depths. Right panel: The histogram of the bubble depth for the entire year (all data) follows an exponential distribution.

low sampling frequency (0.25 Hz) biases the measurements in short-period sea states (where the Nyquist frequency is higher than the dominant wave frequency).

2.1.1. Estimating Bubble Depth

The depth of air bubbles from breaking waves is determined relative to the instantaneous ocean surface elevation (ζ), similar to methods by Gemmrich (2010) and Wang et al. (2016). The backscattered signal is smoothed using a 3×3 spatial filter. The surface is detected below a threshold (here -25 dB, corresponding to the 99th percentile). The thickness D of the bubble layer is defined relative to the sea surface (ζ) as the depth where the backscattered signal drops below -50 dB (Wang et al., 2016). The signal must be above -50 dB continuously to the surface or else it is removed (as it potentially represents a biological signal). Finally, the hourly mean ($\bar{D}$) and maximum (D_{max}) bubbles depth are calculated (Figure 2b) for comparison with observations and wave model parameters. Figures 2c and 2d show the bubble depth variability within 1 month and within 2 hr, respectively. In the example shown in Figure 2d, the wind is approximately 17 m s^{-1} with stable atmospheric conditions and continuous wave breaking. We see that there is a periodicity of larger breaking events of 5–10 min which we attribute to wind gustiness and the natural groupiness of waves.

The long-term probability distribution of bubble depths exhibits an exponential distribution (Figure 3, right panel). In our study we focus on the hourly mean and maximum bubble depths. It is thus of interest to also look at the probability distribution of the intrahourly measurements, that is, how do the 0.25-Hz measurements distribute around their hourly averages? As the sea state and the associated bubble depth vary greatly throughout the yearlong data set, we have standardized the data according to their hourly mean and standard deviation

$$Z_{ij} = \frac{D_{ij} - \bar{D}_i}{s_i}. \tag{1}$$

Here $\bar{D}_i$ represents the hourly average depths, s_i is the hourly standard deviation, and D_{ij} the 0.25-Hz measurements organized in intrahourly chunks of N_i measurements numbered from $j = 1, \ldots, N_i$. The histogram of standardized depth for the month of July 2015 is shown in Figure 3, left panel. The data are skewed toward higher bubble depths, following a weak lognormal distribution. Overlaid on the monthly standardized histogram is the histogram of the storm episode highlighted in Figure 2d. It is clear that the two are very similar, which suggests that a weak lognormal distribution is the norm across a broad range of sea states.

2.2. Wind and Hydrographic Observations

Hourly 10-m wind observations are taken from stations Røst (U_R) at 67.5°N, 012.1°E and Andøya (U_A) at 69.3°N, 016.1°E; see Figure 1. Both are operated by the Norwegian Meteorological Institute. Hydrographic

observations are taken at the Eggum station located offshore of the island Vestvågøy in Lofoten (68.4°N, 013.6°E). The station is operated by the Norwegian Institute of Marine Research. These observations are taken manually two to three times per month with a SAIV SD 204 conductivity-temperature-depth instrument with external water sampler (T. Hovland, personal communication, September 2018). The temperature is calibrated with reversing thermometers, while salinity is calibrated with water samples analyzed in lab. The accuracy is 0.01 for both salinity (PSU) and temperature (K). The mixed layer depth (MLD) is calculated from the potential density profile. The MLD is defined at the point where there is a difference of 0.003 kg m^{-3} in relation to a reference depth of 5 m (to avoid diurnal heating, see de Boyer Montégut et al., 2004).

3. Modeled Wave Parameters

3.1. The EC-WAM Hindcast

Hourly wind (U_{EC}) and wave parameters are taken from a global wave hindcast forced with ERA-Interim 10-m wind (Dee et al., 2011), run by the European Centre for Medium-range Weather Forecasts (ECMWF). The spatial resolution is 0.36°. The spectrum is resolved by 30 frequencies arranged logarithmically between 0.035 and 0.55 Hz and 36 directional bins. The model is set up with source terms as presented by Ardhuin et al. (2010). See also Breivik et al. (2019) for details on the hindcast integration. Wave parameters such as total significant wave height (H_s), wind sea (H_{ws}) and swell (H_{sw}) wave height, drag coefficient (C_d) and the TKE flux (Φ_{oc}) are bilinearly interpolated to the LoVe Observatory location.

3.1.1. Modeled TKE Flux From Breaking Waves

Although the presence of bubbles means that waves dissipate, only a fraction of the total energy lost by the waves contributes directly to upper ocean mixing and manifests itself as bubbles (Melville, 1994). It is not clear exactly how the wave energy loss is partitioned between turbulence in the air (Iafrati et al., 2014), in the water column (Terray et al., 1996, 1997), and as work against buoyancy (Melville, 1994), that is, bubbles. Thomson et al. (2016) found the TKE dissipation to be a decreasing fraction of the total wave dissipation as the sea state increases. Since microscale wave breaking does not entrain air into the water column but contributes to wave energy dissipation (Banner & Phillips, 1974; Sutherland & Melville, 2015), we are not able to measure this part of the energy budget.

However, for fully developed sea state, the TKE flux from breaking waves has traditionally been parameterized as a function of the wind energy input (Craig & Banner, 1994), proportional to the cube of the friction velocity

$$\Phi_{oc,p} = \rho_w \alpha_{CB} u_*^3. \tag{2}$$

Here, ρ_w is the density of seawater, the nondimensional coefficient α_{CB} depends on the sea state (but was assumed constant by Craig & Banner, 1994), or equivalently the wave age (Terray et al., 1996, 1997), and u_* is the waterside friction velocity, defined as $u_* = \sqrt{\tau/\rho_w}$. The wind stress $\tau = C_d \rho_a U_{10}^2$ where ρ_a is the density of the atmosphere, C_d is the drag coefficient, and U_{10} is the local 10-m wind speed. Substituting u_* into equation (2) allows us to estimate Φ_{oc} from the local wind speed U_{10},

$$\Phi_{oc,p} = \sqrt{(\rho_a^3 C_d^3)/\rho_w} \, \alpha_{CB} U_{10}^3. \tag{3}$$

Here, $\rho_a = 1.125$ kgm^{-3} (the standard air density of ERA-Interim), $\rho_w = 1026$ kg m^{-3} (observed mean surface water density at Eggum), $C_d = 1.5 \times 10^{-3}$ (mean), and the nondimensional TKE flux $\alpha_{CB} = 100$, following Craig and Banner (1994). Mellor and Blumberg (2004) suggested a range $50 \leq \alpha_{CB} \leq 150$ from the work by Terray et al. (1996, 1997) and Stacey (1999).

The waves are however normally not in equilibrium with the local wind, and the TKE flux from breaking waves should properly be calculated from the dissipation source term of a spectral wave model (Breivik et al., 2015)

$$\Phi_{oc,m} = -\rho_w g \int_0^{2\pi} \int_0^{\infty} S_{ds} \, d\omega \, d\theta, \tag{4}$$

where g is the gravitational acceleration and S_{ds} is the dissipation source term of the energy balance equation integrated over all frequencies (ω) and directions (θ). The flux, equation (4), is calculated online in EC-WAM.
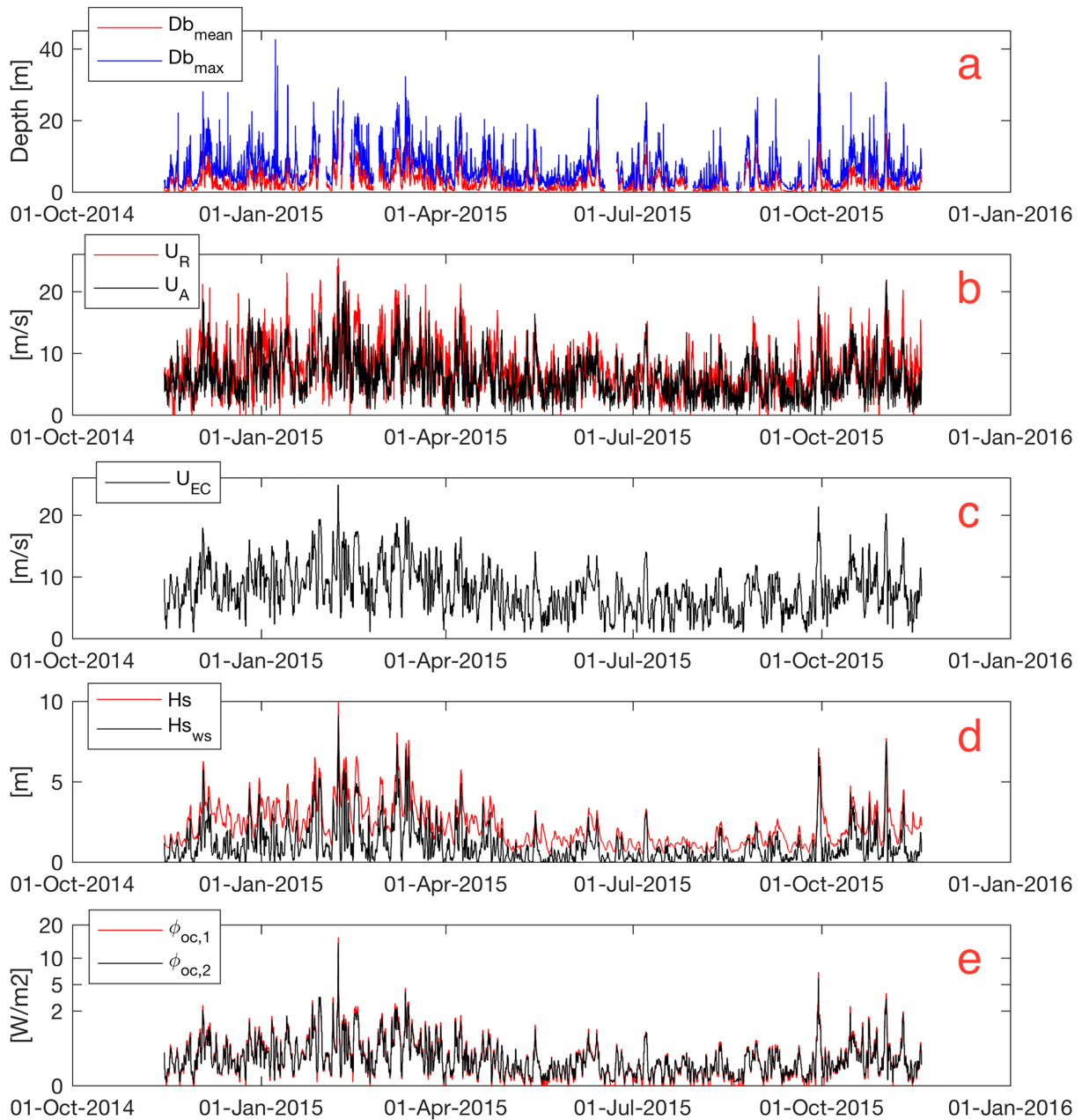
Figure 4. One year of data. (a) Mean ($\bar{D}$) and maximum (D_{max}) bubble depth (m) calculated from EK60 echosounder observations at the LoVe observatory. (b) Observed wind (m s^{-1}) at both Andøya (U_A) and Røst (U_R). (c) Modeled wind (m s^{-1}) from EC-WAM (U_{EC}). (d) Modeled H_s and H_{ws} (m) from EC-WAM. (e) TKE flux (Wm^{-2}) from breaking waves by EC-WAM ($\Phi_{oc,1}$, red) according to equation (4) and parameterized ($\Phi_{oc,2}$, black) according to equation (3). Note that the y axis is cubic.

The subscripts m and p for Φ_{oc} in equations (2)–(4) distinguish between modeled and parameterized estimates. The formulation by Gemmrich et al. (1994) is

$$\Phi_{oc,eff} = \rho_w u_*^2 c_{eff} \quad , \tag{5}$$

where c_{eff} is an estimate of the weighted, effective wave speed that takes into account the sea state and as such yields a more realistic estimate of the TKE flux. Here we choose to rather contrast the wave model TKE flux, equation (4), against equation (2) as it is the simplest possible baseline parameterization of wave dissipation (ignoring sea state).

Table 1

Correlation Coefficients (Pearson's Linear (r_p) and the Spearman Rank (r_s)) Between Observed Mean ($\bar{D}$) and Maximum Bubble Depth (D_{max}) Between the Following Time Series: Wind Speed, U_{10} (From EC-WAM, U_{EC}, Andøya, U_A, and Røst, U_R), Total Significant Wave Height from EC-WAM (H_s) and NORA10EI and Split Between Wind Waves, H_{ws}, and Swell, H_{sw}), and Turbulent Kinetic Energy Flux from Breaking Waves (Φ_{oc} Both Modeled; $\Phi_{oc,m}$ (equation 4), and Estimated From Wind Speed, $\Phi_{oc,p}$ (equation 3) Using Wind Speed (EC-WAM; Φ_{EC} and Andøya; Φ_A)

		Wind speed U_{10}			ECMWF H_s			NORA10EI H_s				Param $\Phi_{oc,p}$	
		U_{EC}	U_A	U_R	H_s	H_{sw}	H_{ws}	H_s	H_{sw}	H_{ws}	ECMWF $\Phi_{oc,m}$	Φ_{EC}	Φ_A
$\bar{D}$	r_p	0.80	0.72	0.60	0.69	0.35	0.84	0.70	0.22	0.87	0.67	0.64	0.67
	r_s	0.80	0.72	0.55	0.64	0.41	0.82	0.64	0.29	0.85	0.81	0.80	0.77
D_{max}	r_p	0.77	0.69	0.58	0.74	0.46	0.82	0.75	0.33	0.84	0.64	0.61	0.64
	r_s	0.77	0.68	0.55	0.74	0.54	0.80	0.74	0.42	0.80	0.79	0.77	0.73

4. The Relationship Between Bubble Depth and Wind and Wave Parameters

Hourly time series of echosounder mean ($\bar{D}$) and maximum (D_{max}) air bubble depth are compared with modeled (U_{EC}) and observed (U_A and U_R) wind speed, modeled wind sea (H_{ws}), swell (H_{sw}), total significant wave height (H_s), and TKE flux from breaking waves from EC-WAM ($\Phi_{oc,m}$) as well as the flux parameterized ($\Phi_{oc,p}$) using wind from EC-WAM and Andøya (Figure 4). We see that $\bar{D}$ varies between 0 and 18 m, while D_{max} varies between 2 and 38 m. The linear correlation between $\bar{D}$ and D_{max} is $r = 0.94$, suggesting that the estimates of maximum hourly bubble depth are quite robust. The fact that D_{max} is more than twice the hourly average illustrates the importance of individual breaking events for the bubble injection.

Before we look at the relationship between the TKE flux from the wave model and the bubble depth, we briefly investigate the sensitivity of the parameterized TKE flux given by equation (3). Varying ρ_a between 1.125 and 1.2 kg m^{-3} (typical atmospheric density range) in equation (3) changes the flux by up to 0.7 Wm^{-2}. Varying ρ_w between 1,025 and 1,027 kgm^{-3} (the surface range observed at Eggum) yields differences of the order of 10^{-3} Wm^{-2}. Finally, varying α_{CB} between 50 and 150 (the typical range suggested by Banner & Phillips, 1974) changes the flux by as much as 6.4 Wm^{-2}. Finally, varying the drag coefficient C_d between 1.5 and 3 $\times$ 10^{-3} gives differences up to 12 Wm^{-2}. It is clear that the uncertainty in the drag coefficient and the dimensionless flux far outstrip uncertainties in density.

Correlation coefficients (Pearson's linear and Spearman's rank correlation; see Press et al., 2007) between the different time series are given in Table 1. The correlation with wind (U_{EC}, U_A, and U_R), H_s and Φ_{oc} is generally higher for $\bar{D}$ than for D_{max}. The linear correlation between $\bar{D}$ (D_{max}) and modeled wind, U_{EC}, is $r = 0.80$ (0.77). Wind sea, H_{ws}, yields the highest correlation coefficient against $\bar{D}$ (D_{max}), $r = 0.84$ (0.82). As expected, the swell wave height (H_{sw}) exhibits significantly weaker correlation. The MLD is usually deeper than the mean bubble depth, with a seasonal variation of 50–75 m in winter and 10–20 m in summer, and only occasionally does D_{max} exceed the MLD. Dividing the time series into four seasons, the correlations between wind (observed U_A and modeled wind U_{EC}) and $\bar{D}$ show either slightly lower or the same strength for summer and winter, and slightly higher or the same for spring and autumn (not shown). The approximately cubic relationship between wind speed and mean (max) bubble depth naturally yields a weak linear correlation coefficient $r = 0.67$ (0.64) between $\bar{D}$ (D_{max}) and modeled TKE flux $\Phi_{oc,m}$. A better estimate for such highly nonlinear relationships is either to take the linear correlation of the cubic root of the flux or to use the rank correlation which is found to be $r = 0.81$ (0.79). A similar rank correlation is found for the parameterized $\Phi_{oc,p}$ (Table 1).

Scatter plots of wind, H_{ws}, and $\Phi_{oc,m}$ against bubble depth ($\bar{D}$ and D_{max}) are shown in Figure 5. The relationship shows the expected near-cubic relationship between modeled Φ_{oc} and bubble depth (both $\bar{D}$ and D_{max}), whereas there is a linear relationship between wind speed and $\bar{D}$ from 4–17 m s^{-1}. D_{max} and wind show a more logarithmic behavior from 7 m s^{-1} up to at least 17 m s^{-1}. For H_{ws} below 5 m there is a linear behavior ($\bar{D} \approx aH_{ws}$, where the factor a is on average 2.4 for H_{ws} and in the range 0.2–6 for H_s).

4.1. Bubble Depth Correlated Against a High-Resolution Hindcast

To assess the impact of atmospheric and wave model resolution, we have also compared the bubble time series with time series of wind and waves from NORA10EI, a high-resolution hindcast archive (Haakenstad et al., 2020) similar to the NORA10 hindcast (Reistad et al., 2011), but forced with downscaled ERA-Interim
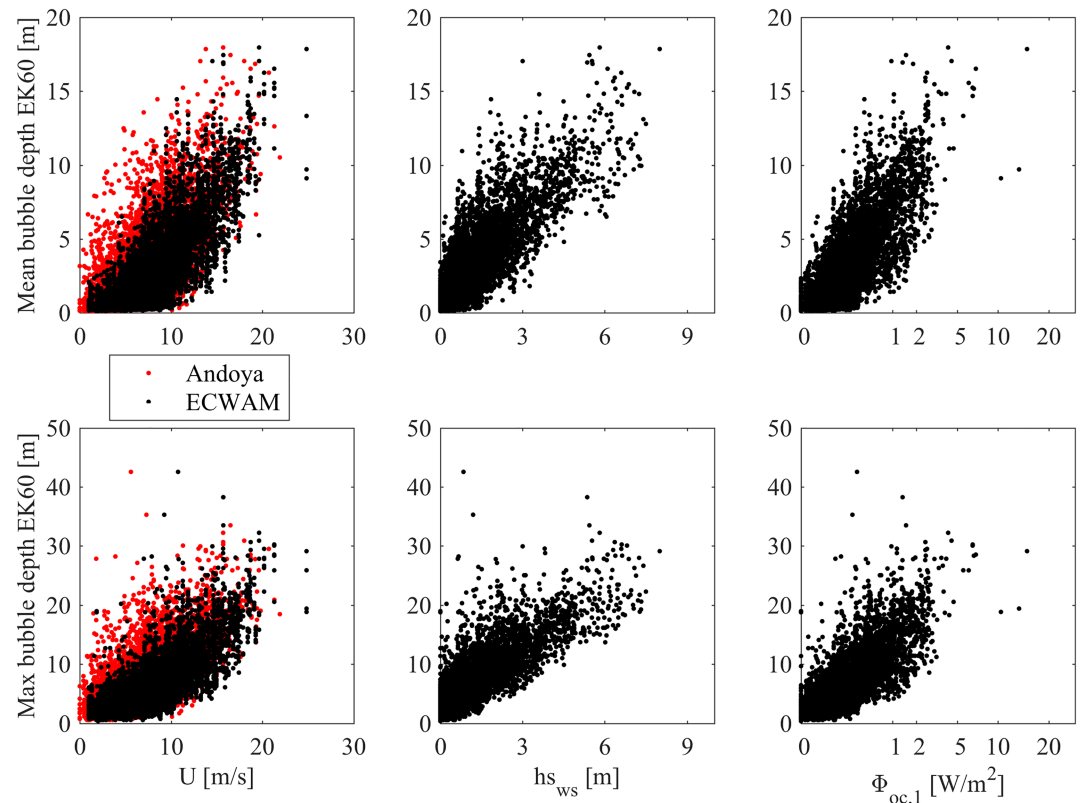
Figure 5. Scatter plot for 1 year of data, for both mean (upper panels) and maximum (lower panels) bubble depths. Left panels show bubble depth against observed wind speed at Andøya (red) and EC-WAM wind (black). Middle panels show bubble depth against modeled EC-WAM wind sea, H_{ws}. Right panels show bubble depth against modeled TKE flux from breaking waves by EC-WAM, $\Phi_{oc,m}$ (Note that the x axis is cubic).

winds rather than ECMWF analyses. It is thus dynamically consistent with the EC-WAM hindcast (40×40-km resolution) which is also forced with ERA-Interim winds. Parameters evaluated from NORA10EI include wind speed (U_{10}), wind sea (H_{ws}), swell (H_{sw}), and total significant wave height (H_s). We also parameterize the TKE flux ($\Phi_{oc,p}$) from the NORA10EI wind speed with variable and constant drag coefficient (C_d). The overall highest linear correlation coefficient with mean and maximum air bubble depth is found against NORA10EI wind ($r = 0.86$ and 0.81, respectively) and H_{ws} ($r = 0.87$ and 0.84, respectively). The NORA10EI parameters H_s and $\Phi_{oc,p}$ with variable C_d exhibit similar linear correlation coefficients compared with same parameters from EC-WAM. Higher model resolution thus appears to strengthen the correlation between modeled parameters and the observed bubble depth, even in open ocean conditions. This is evident in the relationship between the modeled wind sea, H_{ws}, and bubble depth.

5. Discussion

Bottom-mounted echosounder measurements provide a unique opportunity to continuously monitor the upper ocean over long periods and to investigate the interaction between weather, sea state, and the underlying mixed layer. Because air bubbles directly affect backscatter of sound waves, they are easily detected and can be quantified within specific size ranges limited by the frequency of the emitted sound. Bubble depth may inform on dynamical processes including downmixing of buoyant particles due to breaking waves and the entrainment of gases such as carbon dioxide to the ocean interior. To better understand how buoyant particles are distributed in the vertical due to various forcing, we analyzed a year of concurrent measured and modeled wind and modeled waves and wave-induced TKE flux.

The highly variable hourly mean and maximum bubble depths reach maxima of 18 and 38 m during our 1-year time series, respectively. In general, the bubble depth is shallowest during summer following the seasonal variations in wind speed and waves. The correlation between wind and bubble depth is also slightly

weaker in the summer. This may be caused by high biological activity which can obscure the backscattered signal, either through primary production causing supersaturation of oxygen and bubbles in the mixed layer or through high concentrations of zooplankton. The calculated MLD follows a similar seasonal variation as observed by Nilsen and Falck (2006). The summertime MLD may be shallower than maximum bubble depth and is thus not a limiting factor for breaking waves, but we cannot rule out that the density stratification may obscure the wind to bubble depth relationship. Hydrographic observations with same time resolution as the acoustic data would give more conclusive results.

There is a strong correlation between bubble depth and both wind and wave height, in agreement with previous studies (e.g., Wang et al., 2016). The correlation is generally higher for mean bubble depth than for maximum bubble depth. This is expected, as the maximum bubble depth is a noisier parameter than the hourly average bubble depth. However, a linear correlation coefficient of $r = 0.94$ between mean and maximum bubble depth gives confidence in the data processing and the filtering (e.g., removal of ship traffic, as illustrated in Figure 2c). It is also interesting to note that this shows that a much lower sampling frequency than our 0.25 Hz would still yield a good estimate of the average bubble depth. Swell is defined in both wave models (EC-WAM and NORA10EI) as spectral wave components whose propagation vector projected on the local wind vector cannot be sustained by the local wind (ECMWF, 2019),

$$1.2 \times 28(u^*/c)\cos(\theta - \phi) \leq 1. \tag{6}$$

Here u^* is the airside friction velocity and c is the phase speed of the wave component in question. The cosine of the angular difference $\theta - \phi$ between the propagation direction of the waves (θ) and the local wind direction (ϕ) ensures that wave components traveling at large angles to the local wind are classified as swell. These will presumably not contribute to the flux from breaking waves as swell waves have low steepness. The total significant wave height H_s and the swell height H_{sw} should thus exhibit weaker correlation than the wind sea part of the waves, H_{ws}. This is seen in Table 1.

The mean bubble depth is linearly dependent on the wind speed between 4 and 17 m s^{-1}. The lower limit 4 ms^{-1} coincides with the threshold for whitecapping (Callaghan & White, 2009; Hwang & Sletten, 2008; Monahan & O'Muircheartaigh, 1986; Scanlon et al., 2016). Figure 5 indicates that bubble depth is higher than expected in low-wind conditions. This may be a signature of the biological productivity otherwise hidden by the high backscatter of air bubbles from breaking waves. The higher limit of 17 ms^{-1} may partly be related to intense wave breaking in high wind events and partly to ERA-Interim's inability to capture high wind events (Aarnes et al., 2015; Breivik et al., 2014). ERA-Interim wind correlates better with bubble depth than observed wind. This partly reflects not only the high quality of ERA-Interim but also the fact that the wind observations from Andøya and Røst are affected by topographic features and thus less representative for the offshore LoVe location. The overall highest linear correlation is between mean bubble depth and H_{ws}, which is as expected since it is the wind-sea component of the wave field that breaks and causes entrainment of air bubbles. The mean bubble depth is $\bar{D} \approx 2.4 H_{ws}$ (see Figure 5) and between 0.2 and 8 times the total significant wave height, H_s. These relations correspond well with the results of Wang et al. (2016) who found that the mean bubble detph was of the order of $2H_s < \bar{D} < 4H_s$ from 2 weeks of data. Since we have a sampling frequency of 0.25 Hz these results will include an effect of orbital motions for waves with period less than 8 s, similarly assessed by Thomson et al. (2016).

Correlating ranked values can reveal strongly nonlinear relations. For this reason the Spearman rank correlation (Press et al., 2007, pp 749–751) between Φ_{oc} and mean bubble depth is higher than the Pearson linear correlation coefficient (because of the cubic relationship between Φ_{oc} and mean bubble depth; see Figure 5). No clear difference is seen between the TKE flux calculated using $\Phi_{oc,m}$ compared to $\Phi_{oc,p}$, and both show high rank correlation with bubble depth (see Table 1). This may be related to the area investigated, which is located offshore at 68°N where the waves are usually close to full development. A possible follow-up study may thus be to investigate the relationship between the bubble depth and the TKE flux in a fetch-limited area.

6. Concluding Remarks

We have investigated a full year of bubble depth measurements relative to wind, waves, and the TKE flux from breaking waves. The exposed location means that the measurements were taken in sea states ranging

from calm to as much as 10-m significant wave height. Bubble depths show strong correlation with both wind speed and wave height, as reported by previous studies (Thorpe, 1992; Wang et al., 2016). The total significant wave height displays a lower correlation than the wind sea, and the swell is even more weakly correlated (Table 1). This is as expected from physical considerations (swell should not break), but is indirect evidence that the wave model is correctly separating wind sea from swell. We also found that increased resolution strengthens the correlation, as we compare with a high-resolution (10 km) wave hindcast (Haakenstad et al., 2020) forced with the same (ERA-Interim) winds as the coarse (40 km) global wave model run used for the assessment of TKE fluxes (Breivik et al., 2019).

The most important finding is the strong correlation with the modeled energy flux from breaking waves. The fact that the bubble depth correlation is comparable to that against wind speed shows that there is a remarkably strong relation between the energy dissipation parameterized by the wave model and observed bubble depth.

Although we found that the bubble depth exhibits a strong relationship with the TKE flux from breaking waves, we cannot conclude on exactly how the energy from dissipating waves is partitioned between turbulence production in the air and water and work against buoyancy. An important avenue of further research is to quantify the energy budget of breaking waves and how it is split between generation of bubbles and processes such as microbreaking that do not generate bubbles (Melville, 1994; Melville & Matusov, 2002). Being able to do so would benefit both ocean and wave models. The latter because at present the dissipation terms are not calibrated separately (see Tsagareli et al., 2010), the former because it would allow a more precise estimate of the turbulence production in the active breaking zone of the mixed layer. However, because of the strong correlation between the TKE flux from breaking waves and the observed bubble depth, it seems likely that the fraction of energy that goes into bubble production is relatively constant over a broad range of sea states.
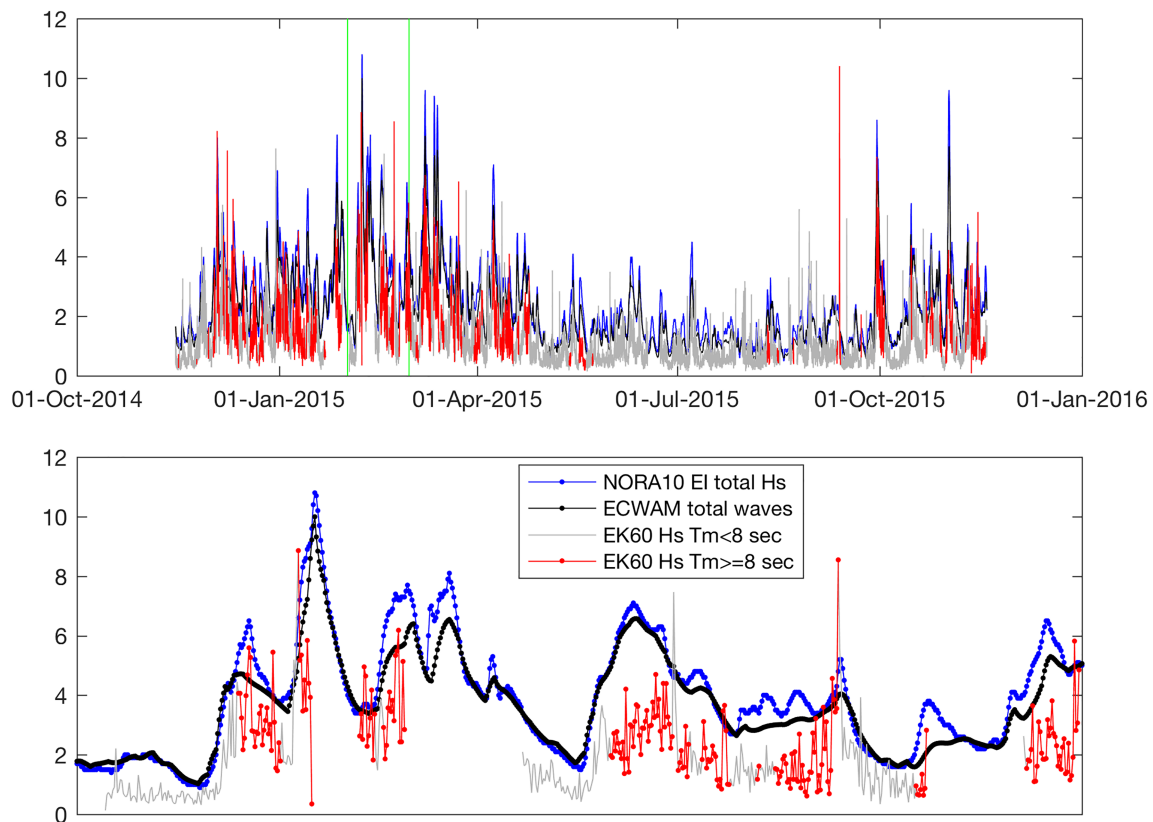

Figure A1. Hourly data of total significant wave heights (H_s) from NORA10EI (blue), EC-WAM (black), H_s estimated by the EK60 with NORA10EI wave period $T_{m_{02}}$, below 8 s (gray), and with $T_{m_{02}}$ above 8 s (red); see legend in lower panel. Upper panel: One year of data from 14 November 2014 to 18 November 2015. Two green vertical lines mark the period in panel below. Lower panel: Zoom on February 2015.

Appendix A: Estimating Significant Wave Height From the EK60 EchoSounder

The instantaneous ocean surface elevation (ζ) is detected by the EK60 echosounder. This allows us to make an estimate of H_s. First, the mean value is subtracted from the time series to get values around zero at the surface. Second, the tidal variability is removed using the `t_tide` MATLAB toolbox (Pawlowicz et al., 2002). Hourly averages of significant wave height were estimated from the standard deviation of elevation, $H_s = 4$ std (ζ). The correlation between modeled H_s from NORA10EI and H_s estimated from EK60 is $r = 0.72$. Since the sampling frequency of the EK60 echosounder is 0.25 Hz, the Nyquist frequency is 0.125 Hz, and the instrument is thus only able to capture waves with periods of 8 s or longer. The peak period was found to be longer than 8 s about 30% of the time. If the sampling frequency had been increased to 0.5 Hz, 80% of the waves would be captured. In Figure A1 the time series of measured H_s is shown in red where the NORA10EI mean wave period $T_{m_{02}}$ exceeds 8 s. The mean observed wave height is biased low, but the correlation with modeled wave height is quite high, exceeding 0.8 against both EC-WAM and NORA10EI.

References

Aarnes, O. J., Abdalla, S., Bidlot, J.-R., & Breivik, Ø. (2015). Marine wind and wave height trends at different ERA-Interim forecast ranges. *Journal Climate*, *28*, 819–837.

Aarnes, O. J., Breivik, Ø., & Reistad, M. (2012). Wave extremes in the Northeast Atlantic. *Journal Climate*, *25*, 1529–1543.

Alari, V., Staneva, J., Breivik, Ø., Bidlot, J.-R., Mogensen, K., & Janssen, P. (2016). Surface wave effects on water temperature in the Baltic Sea: Simulations with the coupled NEMO-WAM model. *Ocean Dynamics*, *66*, 917–930.

Ali, A., Christensen, K., Breivik, Ø, Malila, M, Raj, R., Bertino, L, et al. (2019). A comparison of Langmuir turbulence parameterizations and key wave effects in a numerical model of the North Atlantic and Arctic Oceans. *Ocean Modelling*, *137*, 76–97.

Ardhuin, F., Rogers, E., Babanin, A. V., Filipot, J.-F., Magne, R., Roland, A., et al. (2010). Semiempirical dissipation source functions for ocean waves. Part I: Definition, calibration, and validation. *Journal of Physical Oceanography*, *40*(9), 1917–1941.

Banner, M. L., & Phillips, O. (1974). On the incipient breaking of small scale waves. *Journal of Fluid Mechanics*, *65*(4), 647–656.

Belcher, S. E., Grant, A. L., Hanley, K. E., Fox-Kemper, B., Van Roekel, L., Sullivan, P. P., et al. (2012). A global perspective on Langmuir turbulence in the ocean surface boundary layer. *Geophysical Research Letters*, *39*, L18605. https://doi.org/10.1029/2012GL052932

Bell, T. G., Landwehr, S., Miller, S. D., de Bruyn, W. J., Callaghan, A. H., Scanlon, B., et al. (2017). Estimation of bubble-mediated air-sea gas exchange from concurrent DMS and CO_2 transfer velocities at intermediate-high wind speeds. *Atmospheric Chemistry and Physics*, *17*(14), 9019–9033.

Breivik, Ø., Aarnes, O., Abadalla, S, Bidlot, J.-R., & Janssen, P. (2014). Wind and wave extremes over the world oceans from very large ensembles. *Geophysical Research Letters*, *41*, 5122–5131. https://doi.org/10.1002/2014GL060997

Breivik, Ø., Aarnes, O. J., Bidlot, J.-R., Carrasco, A., & Saetra, Ø. (2013). Wave extremes in the northeast Atlantic from ensemble forecasts. *Journal Climate*, *26*, 7525–7540.

Breivik, Ø., Carrasco, A., Staneva, J., Behrens, A., Semedo, A., Bidlot, J.-R., & Aarnes, O. J. (2019). Global stokes drift climate under the RCP8.5 scenario. *Journal Climate*, *32*(6), 1677–1691.

Breivik, Øyvind, Mogensen, K., Bidlot, J.-R., Balmaseda, M. A., & Janssen, P. A. E. M. (2015). Surface wave effects in the NEMO ocean model: Forced and coupled experiments. *Journal of Geophysical Research: Oceans*, *120*, 2973–2992. https://doi.org/10.1002/2014JC010565

Burchard, H. (2001). Simulation the wave-enhanced layer under breaking surface waves with two-equation turbulence models. *Journal of Physical Oceanography*, *31*(11), 3133–3145.

Callaghan, A. H. (2018). On the relationship between the energy dissipation rate of surface-breaking waves and oceanic whitecap coverage. *Journal of Physical Oceanography*, *48*(11), 2609–2626.

Callaghan, A. H., Deane, G., & Stokes, M. (2016). Laboratory air-entraining breaking waves: Imaging visible foam signatures to estimate energy dissipation. *Geophysical Research Letters*, *43*, 11–320. https://doi.org/10.1002/2016GL071226

Callaghan, A. H., & White, M. (2009). Automated processing of sea surface images for the determination of whitecap coverage. *Journal Atmospheric and Oceanic Technology*, *26*(2), 383–394.

Clay, C. S., & Medwin, H. (1977). *Acoustical oceanography: Principles and applications*. New York, NY (USA): Wiley-Interscience.

Colbo, K., Ross, T., Brown, C., & Weber, T. (2014). A review of oceanographic applications of water column data from multibeam echosounders. *Estuarine, coastal and shelf science*, *145*, 41–56.

Craig, P. D., & Banner, M. L. (1994). Modeling wave-enhanced turbulence in the ocean surface layer. *Journal of Physical Oceanography*, *24*(12), 2546–2559.

de Boyer Montégut, C., Madec, G., Fischer, A. S., Lazar, A., & Iudicone, D. (2004). Mixed layer depth over the global ocean: An examination of profile data and a profile-based climatology. *Journal of Geophysical Research*, *109*, C12003. https://doi.org/10.1029/2004JC002378

Dee, D., Uppala, S., Simmons, A., Berrisford, P., Poli, P., Kobayashi, S., et al. (2011). The ERA-Interim reanalysis: Configuration and performance of the data assimilation system. *Quarterly Journal of the Royal Meteorological Society*, *137*(656), 553–597.

Demer, D., Berger, L., Bernasconi, M., Bethke, E., Boswell, K., Chu, D., et al. (2015). Calibration of acoustic instruments. *ICES Cooperative Research Report*, *326*, 133.

ECMWF (2019). IFS documentation CY46r1, Part VII: ECMWF wave model.

Esters, L., Breivik, Ø., Landwehr, S., A ten Doeschate, G. S., Christensen, K., Bidlot, J-R, & Ward, B (2018). Turbulence scaling comparisons in the ocean surface boundary layer. *Journal of Geophysical Research: Oceans*, *123*, 2172–2191. https://doi.org/10.1002/2017JC013525

Esters, L., Landwehr, S, Sutherland, G, Bell, T. G., Christensen, K. H., Saltzman, E. S., et al. (2017). Parameterizing air-sea gas transfer velocity with dissipation. *Journal of Geophysical Research: Oceans*, *122*, 3041–3056. https://doi.org/10.1002/2016JC012088

Fan, Y., & Griffies, S. M. (2014). Impacts of parameterized Langmuir turbulence and non-breaking wave mixing in global climate simulations. *Journal Climate*, *27*, 4752–4775.

Fisher, A. W., Sanford, L. P., & Scully, M. E. (2018). Wind-wave effects on estuarine turbulence: A comparison of observations and second-moment closure predictions. *Journal of Physical Oceanography*, *48*(4), 905–923.

Foote, K. G. (1987). Calibration of acoustic instruments for fish density estimation: A practical guide. *ICES Cooperative Research Report*, *144*, 1–69.

Gemmrich, J. (2010). Strong turbulence in the wave crest region. *Journal of Physical Oceanography*, *40*(3), 583–595.

Gemmrich, J. R., & Farmer, D. M. (1999). Observations of the scale and occurrence of breaking surface waves. *Journal of Physical Oceanography*, *29*(10), 2595–2606.

Gemmrich, J., Mudge, T., & Polonichko, V. (1994). On the energy input from wind to surface waves. *Journal of Physical Oceanography*, *24*(11), 2413–2417.

Haakenstad, H, Breivik, Ø, Reistad, M, & Aarnes, O. (2020). NORA10EI: A revised regional atmosphere-wave hindcast for the North Sea, the Norwegian Sea and the Barents Sea. *International Journal of Climatology*, *40*, 1–27.

Hwang, P. A., & Sletten, M. A. (2008). Energy dissipation of wind-generated waves and whitecap coverage. *Journal of Geophysical Research*, *113*, C02012. https://doi.org/10.1029/2007JC004277

Iafrati, A, Babanin, A, & Onorato, M. (2014). Modeling of ocean-atmosphere interaction phenomena during the breaking of modulated wave trains. *Journal of Computational Physics*, *271*, 151–171.

Jones, C., Dagestad, K.-F., Breivik, Ø., Holt, B., Röhrs, J., Christensen, K., et al. (2016). Measurement and modeling of oil slick transport. *Journal of Geophysical Research: Oceans*, *121*, 7759–7775. https://doi.org/10.1002/2016JC012113

Lamont, J. C., & Scott, D. (1970). An eddy cell model of mass transfer into the surface of a turbulent liquid. *AIChE Journal*, *16*(4), 513–519.

Li, Q, Fox-Kemper, B, Breivik, Ø, & Webb, A (2017). Statistical models of global Langmuir mixing. *Ocean Modelling*, *113*, 95–114.

Li, Q., Webb, A., Fox-Kemper, B., Craig, A., Danabasoglu, G., Large, W. G., & Vertenstein, M. (2016). Langmuir mixing effects on global climate: WAVEWATCH III in CESM. *Ocean Modelling*, *103*, 145–160.

Melle, W., Ellertsen, B., & Skjoldal, H. R. (2004). Zooplankton: The link to higher trophic levels. *The Norwegian Sea Ecosystem*, 137–202.

Melle, W., & Skjoldal, H. R. (1998). Reproduction and development of Calanus finmarchicus, C. glacialis and C. hyperboreus in the Barents Sea. *Marine Ecology Progress Series*, *169*, 211–228.

Mellor, G., & Blumberg, A. (2004). Wave breaking and ocean surface layer thermal response. *Journal of Physical Oceanography*, *34*(3), 693–698.

Melville, K. (1994). Energy dissipation by breaking waves. *Journal of Physical Oceanography*, *24*(10), 2041–2049.

Melville, WKendall, & Matusov, P. (2002). Distribution of breaking waves at the ocean surface. *Nature*, *417*(6884), 58.

Monahan, E. C., & O'Muircheartaigh, I. G. (1986). Whitecaps and the passive remote sensing of the ocean surface. *International Journal of Remote Sensing*, *7*(5), 627–642.

Nilsen, JanEvenØie, & Falck, E. (2006). Variations of mixed layer properties in the Norwegian Sea for the period 1948–1999. *Progress in Oceanography*, *70*(1), 58–90.

Paris, C. B., HÃİnaff, M. L., Aman, Z. M., Subramaniam, A., Helgers, J., Wang, D.-P., et al. (2012). Evolution of the macondo well blowout: Simulating the effects of the circulation and synthetic dispersants on the subsea oil transport. *Environmental science and technology*, *46*(24), 13,293–13,302.

Pawlowicz, R., Beardsley, B., & Lentz, S. (2002). Classical tidal harmonic analysis including error estimates in MATLAB using t_tide. *Computers & Geosciences*, *28*(8), 929–937.

Press, W. H., Teukolsky, S. A., Vetterling, W. T., & Flannery, B. P. (2007). *Numerical recipes in C, 3rd edition*. Cambridge: Cambridge University Press.

Reistad, M., Breivik, Øyvind, Haakenstad, H., Aarnes, O. J., Furevik, B. R., & Bidlot, J.-R. (2011). A high-resolution hindcast of wind and waves for the North Sea, the Norwegian Sea, and the Barents Sea. *Journal of Geophysical Research*, *116*, C05019. https://doi.org/10.1029/2010JC006402

Rhein, M., Rintoul, S. R., Aoki, S., Campos, E., Chambers, D., Feely, R. A., et al. (2013). Observations: Ocean. In T. F. Stocker et al. (Eds.), *Climate Change 2013: The Physical Science Basis. Contribution of Working Group I to the Fifth Assessment Report of the Intergovernmental Panel on Climate Change* (pp. 255–316). Cambridge, UK: Cambridge University Press.

Scanlon, B., Breivik, Øyvind, Bidlot, J.-R., Janssen, P. A., Callaghan, A. H., & Ward, B. (2016). Modeling whitecap fraction with a wave model. *Journal of Physical Oceanography*, *46*(3), 887–894.

Stacey, M. W. (1999). Simulation of the wind-forced near-surface circulation in Knight Inlet: A parameterization of the roughness length. *Journal of Physical Oceanography*, *29*, 1363–1367.

Staneva, J., Alari, V., Breivik, Ø., Bidlot, J.-R., & Mogensen, K. (2017). Effects of wave-induced forcing on a circulation model of the North Sea. *Ocean Dynamics*, *67*, 81–101.

Sund, O. (1935). Echo sounding in fishery research. *Nature*, *135*(3423), 953.

Sundby, S. (1983). A one-dimensional model for the vertical distribution of pelagic fish eggs in the mixed layer. *Deep Sea Research Part A. Oceanographic Research Papers*, *30*(6), 645–661.

Sutherland, P., & Melville, W. K. (2015). Field measurements of surface and near-surface turbulence in the presence of breaking waves. *Journal of Physical Oceanography*, *45*(4), 943–965.

Terray, E., Donelan, M., Agrawal, Y., Drennan, W., Kahma, K., Williams, A., et al. (1996). Estimates of kinetic energy dissipation under breaking waves. *Journal of Physical Oceanography*, *26*(5), 792–807.

Terray, E., Donelan, M., Agrawal, Y., Drennan, W., Kahma, K., Williams III, A., et al. (1997). Reply. *Journal of Physical Oceanography*, *27*(10), 2308–2309.

Thomson, J., Schwendeman, M. S., Zippel, S. F., Moghimi, S., Gemmrich, J., & Rogers, WErick (2016). Wave breaking turbulence in the ocean surface layer. *Journal of Physical Oceanography*, *46*(6), 1857–1870.

Thorpe, S. (1982). On the clouds of bubbles formed by breaking wind-waves in deep water, and their role in air-sea gas transfer. *Philosophical Transactions of the Royal Society of London. Series A, Mathematical and Physical Sciences*, *304*(1483), 155–210.

Thorpe, S. (1984). On the determination of Kv in the near-surface ocean from acoustic measurements of bubbles. *Journal of Physical Oceanography*, *14*(5), 855–863.

Thorpe, S. (1992). Bubble clouds and the dynamics of the upper ocean. *Quarterly Journal of the Royal Meteorological Society*, *118*(503), 1–22.

Trevorrow, M. V. (2003). Measurements of near-surface bubble plumes in the open ocean with implications for high-frequency sonar performance. *Journal of the Acoustical Society of America*, *114*(5), 2672–2684.

Tsagareli, K. N., Babanin, A. V., Walker, D. J., & Young, I. R. (2010). Numerical investigation of spectral evolution of wind waves. Part I: Wind-input source function. *Journal of Physical Oceanography*, *40*(4), 656–666. https://doi.org/10.1175/2009JPO4345.1

Vagle, S., & Farmer, D. M. (1992). The measurement of bubble-size distributions by acoustical backscatter. *Journal of Atmospheric and Oceanic Technology*, *9*(5), 630–644.

Wang, D., Wijesekera, H., Jarosz, E, Teague, W., & Pegau, W. (2016). Turbulent diffusivity under high winds from acoustic measurements of bubbles. *Journal of Physical Oceanography*, *46*(5), 1593–1613.

Wu, L., Rutgersson, A., & Breivik, Ø. (2019). Ocean-wave-atmosphere interaction processes in a fully coupled modelling system. *Journal of Advances in Modeling Earth Systems*, *11*, 3852–3874. https://doi.org/10.1029/2019MS001761

Wu, L., Staneva, J., Breivik, Ø., Rutgersson, A., Nurser, A. J. G., Clementi, E., & Madec, G. (2019). Wave effects on coastal upwelling and water level. *Ocean Modelling*, *140*, 101405, 16pp.

Zappa, C. J., McGillis, W. R., Raymond, P. A., Edson, J. B., Hintsa, E. J., Zemmelink, H. J., et al. (2007). Environmental turbulent mixing controls on air-water gas exchange in marine and aquatic systems. *Geophysical Research Letters*, *34*, L10601. https://doi.org/10.1029/2006GL028790

Zippel, S. F., Thomson, J., & Farquharson, G. (2018). Turbulence from breaking surface waves at a river mouth. *Journal of Physical Oceanography*, *48*(2), 435–453.